

The geometric model-based patient-specific simulations of turbulent aortic valve flows

E. STUPAK¹), R. KAČIANAUSKAS¹), A. KAČENIAUSKAS¹),
V. STARIKOVIČIUS¹), A. MAKNICKAS¹), R. PACEVIČIUS¹),
M. STAŠKŪIENĖ¹), G. DAVIDAVIČIUS²), A. AIDIETIS²)

¹) *Vilnius Gediminas Technical University
Vilnius, Lithuania*

*e-mails: eugenius.stupak@vgtu.lt, rimantas.kacianauskas@vgtu.lt,
arnas.kaceniauskas@vgtu.lt, vadimas.starikovicius@vgtu.lt,
algirdas.maknickas@vgtu.lt, ruslan.pacevic@vgtu.lt,
migle.staskuniene@vgtu.lt*

²) *Vilnius University Hospital “Santariškių Klinikos”
Vilnius, Lithuania*

e-mails: giedrius.davidavicius@santa.lt, audrius.aidietis@santa.lt

THIS PAPER PRESENTS THE PATIENT-SPECIFIC SIMULATIONS of the aortic valve based on the proposed geometric model. A structural analysis is performed by using the finite element method to determine the stress-strain state of the aortic valve. The study is focused on the investigation of various turbulence models crucial for the appropriate description of the flow in the deceleration phase, following the peak systole. A comparative study of the flow solution without a turbulence model and the numerical results obtained by using various turbulence models is also performed. The results yielded by the shear-stress transport $k-\omega$ model supplemented with the intermittency transition equation most closely match those of numerical simulations without a turbulence model.

Key words: geometric model of the aortic valve, pulsatile turbulent flow, shear-stress transport $k-\omega$ model, intermittency transition, finite volume method, finite element method.

Copyright © 2017 by IPPT PAN

1. Introduction

HEART DISEASES ARE THE LEADING CAUSE OF HUMAN DEATHS in the world. The highest standardized death rates from the cardiovascular diseases were often recorded in Eastern Europe [1]. The aortic stenosis is one of the most common valvular disorders encountered in clinical practice, and its prevalence is expected to increase in Europe and North America [2]. The assessment of the aortic stenosis severity is still a challenge for researchers because the definition of severe

stenosis has changed during the past years and differs from one guideline to another [3]. Severe aortic stenosis is usually defined in terms of the aortic valve area and the mean pressure gradient. However, discrepancies are frequently observed between the mean gradient and the valve area in a single patient [4]. They may potentially lead to underestimation of the stenosis and symptom severity and thus to inappropriate delay of the aortic valve replacement, which may have a negative impact on the patient's outcome. These patients represent the most challenging category with respect to the appropriate diagnostic and therapeutic management [5].

The velocity and pressure field of the valve flow are the main quantities of interest for the assessment of stenotic severity. Sufficiently accurate computational models combined with medical imaging can serve as an alternative tool for medical research providing a better quantitative knowledge of the heart flow haemodynamics required for improving the diagnostic and patient care [6]. In this context, the use of computational fluid dynamics (CFD) has gained relevance for the heart valve assessment [7]. It has been shown that the combination of CFD and medical imaging techniques can be highly effective in studying complex cardiovascular dynamics and can provide the detailed haemodynamic information that is unobtainable by using the direct measurement techniques [8, 9]. Despite the progress in the numerical methods and the constantly increasing power of modern computers, the considered problem is still very challenging, owing to complex moving geometries, intrinsic flow unsteadiness and very intense velocity gradients [9].

Two different approaches are currently used for the numerical solution of the considered problem. Models taking into account the fluid-structure interaction (FSI) are very promising. The first attempt to model the FSI problem was undertaken by PESKIN [10], who introduced the immersed boundary method. This method was extended to include the 3D problems and applied to several valve and heart simulations. The fictitious domain is another variant of the Eulerian method, in which the influence of the wall on the flow is imposed by using the velocity constraints only. A few studies employed the fictitious domain method in the FSI simulations of the aortic valve [11, 12], but none of them succeeded in employing physiological boundary conditions. The experimental validation of FSI computations applied to a two-dimensional aortic valve model was demonstrated by DE HART [12]. The of the 3D patient-specific aortic root and valve was presented by NICOSIA *et al.* [13]. The computations were made in an uncoupled manner and took into account the opening and closing behaviour. The aortic valve and root were modelled using the Hughes–Liu shell elements with linear elastic material behaviour. For stability reasons, the peak diastolic pressure was reduced. The initial FSI analyses of the heart valves [12, 13] were restricted to non-physiological flow regimes due to computational challenges. More recently,

the attempts to investigate the coupled interaction of valves with the complex haemodynamic environment in anatomic, patient-specific domains was also made in [14]. With the advent of massively parallel computational platforms, continuous algorithmic advances of separate numerical codes and FSI coupling [15, 16], and the 3D FSI simulations of the heart valves in patient-specific left heart anatomies could be performed [17]. The review on the coupled multiscale and multiphysics models for the simulation of the cardiac function, including the cardiac electrophysiology system as well as the haemodynamics inside the heart chambers were presented by QUARTERONI *et al.* [18]. However, the FSI computations require profound knowledge of the complex tissue rheology [19], the electrical properties [20] or even the external load due to the surrounding organs [9]. It is hardly possible to obtain the required data in a non-invasive way today.

An alternative approach based on the geometry extracted from medical images seems to be better suited for patient-specific analysis and is compatible with clinical routine [9]. With the advent of ultrasound, computer tomography and magnetic resonance imaging modalities, as well as with advances in image processing techniques, it is now possible to obtain patient-specific, morphologically realistic 3D images of the heart valves at various time instances in the cardiac cycle. Therefore, a patient-specific structural and haemodynamic analysis is being increasingly used in biomechanics of blood circulation. The initial attempts to simulate the blood flow in the heart chambers were based on simplified geometries, e.g., straight axisymmetric aortic lumens [21]. BLUESTEIN *et al.* [22] have performed the 2D unsteady turbulent simulations of the mechanical valve for the fixed leaflet position to study platelet activation. MARQUEZ *et al.* [23] have shown that different aortic valve geometries have significantly different haemodynamics in the valve wake. A series of the valve leaflet deformed geometries, from the valve opening to the valve closure, were extracted from the finite element simulation and used to create a series of haemodynamic models by SIROIS *et al.* [6].

The aortic valve has a complex 3D geometry, which is composed of three leaflets and Valsalva sinuses connected together through the commissures. The patient-specific aortic valve geometry can be reconstructed directly from in vivo echocardiography, magnetic resonance imaging or computed tomography measurements [24]. These models can incorporate patient-specific realism to a high degree, provided that imaging modalities of sufficient resolution are available to accurately reconstruct the valve motion [25]. A temporal interpolation between successive images must be used to reconstruct the geometry motion over the cardiac cycle. Obviously, the accuracy of the resulting kinematics and, consequently, the clinical relevance of the 3D haemodynamic model both depend on the accuracy of the interpolation technique and the initial temporal resolution of the acquired images. The present-day scanning frequency per heartbeat is technolog-

ically limited; therefore, the current in-vivo methods for representing the moving aortic valve benefit from the application of the predefined geometric model described by parametric curves. Past geometric descriptions of the aortic root were two-dimensional [26]. A 3D representation of the aortic valve was introduced by THUBRIKAR [27] for designing the trileaflet prosthetic valves. Even though this model was developed for prosthetic valves, a recent study by this group [28] has extended the parametric description of the native valves' post valve-sparing procedures. CLAIBORNE *et al.* [29] have suggested optimizing polymeric prosthetic valves by manufacturing them with variable thickness; however, a mathematical description of their geometry was not provided. RANKIN *et al.* [30] have described the surfaces of the leaflets as three identical hemispheres and the commissures as a cylinder of the same calibre. Most of the discussed studies that used parametric relationships to describe the aortic valve geometry have focused on the cusps and the commissures, but have not included the geometry of the sinuses. Recently, HAJ-ALI *et al.* [31] have suggested a simple 3D geometrical representation of the native trileaflet aortic valve, comprising the leaflets and the root. Two independent parametric curves defined the cusp and one represented the sinuses, while some additional dependent curves have also been generated to join the cusps and the sinuses. The proposed parametric model was also employed to describe different geometries of bicuspid aortic valves [32].

At physiological flow rates, the flow through the aortic valve is known to become turbulent when the fluid jet expands downstream of the valve. Under the pulsatile flow conditions, the turbulence is intermittent, peaking only in the deceleration phase, following the peak systole [33]. This turbulence is known to be a predominant factor, influencing the energy losses caused by the aortic stenosis. Consequently, 3D models have no predictive value for the aortic stenosis, as long as turbulence is not properly described. Various turbulence models of the Reynolds-averaged Navier–Stokes (RANS) equations were employed in mechanical prosthetic aortic valve simulations. KIRIS *et al.* [34] have used a finite volume method with overset grids to solve the 3D RANS equations closed with the mixing-length turbulence model for simulating the flow through the Björk–Shiley mechanical valve. In their turbulence model, the turbulent viscosity is determined only by the profile of the boundary layer and the distance from the wall. BLUESTEIN *et al.* [22, 35] have employed Wilcox k - ω model in simulations of mechanical valves because this turbulence model is better suited for the low Reynolds number transitional flows. Transient and turbulent simulation [35] depicted the intricate dynamics of the shed vortices in the wake, with the results validated using a digital particle image velocimetry. SIROIS *et al.* [6] have performed a quantitative analysis of haemodynamics before and after the transcatheter-aortic valve intervention by using the k - ε model to describe the turbulent flow in the transition range. In the direct numerical simulation (DNS),

full Navier–Stokes equations have been solved without any averaging or assumptions about the production and dissipation of turbulence [36]. The DNS method has been employed in the models of the pulsatile flow through bileaflet mechanical heart valves (MHV), including the valves with the fixed leaflets [37] and full FSI simulations [7, 38]. The DNS of the pulsatile flow through a bileaflet MHV mounted in an idealized axisymmetric aorta geometry has been carried out in [39] by prescribing the leaflet motion from the experimental data. However, the DNS approach requires very fine temporal and spatial discretization and, consequently, very large computational resources because the selected mesh resolution is usually lower than the Kolmogorov scale. Moreover, turbulent models are rarely applied to patient-specific simulations of the native aortic valve flows. Hence, the validation of these models for clinically relevant problems is expected to be the topic of future research.

Simulation of a cardiac cycle is largely related to evaluation of age-matched material properties and numerical models. From the point of view of material behaviour the aortic valve structure was characterized by elastic behaviour [13] or strong nonlinearity of strain-stress relationship [19]. AURICCHIO *et al.* [40] modified Holzapfel’s model [41] taking into account anisotropy and good fit to experimental data in both directions of the native aortic valve. Aortic walls and leaflets were considered as thin structures and were often modelled by using membrane and shell elements [6, 13, 32, 38] in finite element analysis (FEA). NICOSIA *et al.* [13] modelled the aortic valve and root by using Hughes–Liu shell elements with linear elastic material behaviour. The uncoupled computations considered the opening and closing behaviour. In the last few years, modified hyper-elastic nonlinear rotational-free shell elements were proposed [42]. The application of shell elements could help reducing the needed computational power because it employs only five degrees of freedom in each node. Even though it is a common assumption in structural models, shell meshes might present additional challenges in FSI models, particularly those that apply the flow pressure load on each side of the valve. There is only a single node in the thickness; therefore, it might be impossible to define separate pressures on each side since the flow model can usually calculate only a single pressure value in each location, which leads to zero pressure difference on the leaflet. MAROM *et al.* [43] suggested to overcome this problem by adding virtual surfaces on each side of the leaflet, which can represent the real outer surfaces of the leaflets. In this method, the main idea was to transfer the flow-pressure load from the virtual surfaces, or virtual thickness, to the shell nodes. Thus, the local outer forces on the shell nodes were based on the pressure gradient, as they should be. Obviously, each virtual node should move with the corresponding shell node of the finite element model, for example, by rigid body motion based on the displacement and rotation of the specific shell node. Another challenge is the definition of stress-free

configuration, which might not exist in native valves. Recently, 3D models using volume elements have been used for aorta modelling [44, 45].

The present work aims to delineate the important systolic turbulent flow features, obtained in the patient-specific aortic valve computations, based on the proposed 3D geometric model. A comparative study of various turbulence models is presented for the case of the haemodynamic analysis. Other parts of the paper are organized as follows: Section 2 presents the mathematical model used in the analysis, Section 3 describes the patient-specific aortic valve problem, including the novel geometric model based on the parametric curves, Section 4 contains details of the numerical model, while Section 5 provides the FEA of the valve leaflets as well as the simulation results of the turbulent flow through the aortic valve, and Section 6 gives the concluding remarks.

2. Governing equations

A transient flow of viscous incompressible fluid was described by the Navier–Stokes equations as follows [46, 47]:

$$(2.1) \quad \rho \frac{\partial \mathbf{u}}{\partial t} + \rho \mathbf{u} \cdot \nabla \cdot \mathbf{u} = \nabla \cdot \boldsymbol{\sigma},$$

$$(2.2) \quad \nabla \cdot \mathbf{u} = 0,$$

where \mathbf{u} is the velocity vector, ρ is density, ∇ is the gradient operator, $\nabla \cdot$ is the divergence operator. In the case of the Newtonian incompressible fluid, stress tensor $\boldsymbol{\sigma}$ can be expressed by the formula:

$$(2.3) \quad \sigma_{ij} = -p\delta_{ij} + \mu_e \left(\frac{\partial u_i}{\partial x_j} + \frac{\partial u_j}{\partial x_i} \right),$$

where p is pressure, μ_e is effective viscosity, and δ_{ij} is Kronecker delta. The Newtonian flow model was considered, since the blood in the aorta and large arteries behaves accordingly [48]. The non-Newtonian blood behaviour becomes relevant only in the cases of slow flows in the capillaries, whose diameter can be even smaller than that of a red cell, but they are not relevant to our study.

The need for turbulence modelling arises because the local Reynolds number of the blood flow past the aortic valve might reach high values in the deceleration phase, following the peak systole [33]. In this work, the two-equation shear-stress transport (SST) k - ω model [49] was used to avoid the explicit simulation of the smallest scales, because it could be applied for the computation of the turbulent flows with a relatively low Reynolds number. The RANS equations used for turbulence modelling have the same general form as the instantaneous Navier–Stokes equations (2.1)–(2.3), with the time-averaged velocities and the Reynolds

stresses that can be incorporated into the stress description (2.3) by using the effective viscosity:

$$(2.4) \quad \mu_e = \mu + \mu_t,$$

where μ is the viscosity coefficient and μ_t is turbulent viscosity. The SST k - ω model accounts for the transport of the turbulent shear stress, introducing a limiter α to the formulation of turbulent viscosity:

$$(2.5) \quad \mu_t = \frac{1}{\alpha} \frac{\rho k}{\omega},$$

where k is turbulent kinetic energy and ω is the specific dissipation rate. The proper transport behaviour of the turbulent shear stress was obtained, specifying

$$(2.6) \quad \alpha = \max \left[\frac{1}{\alpha^*}, \frac{SF}{a_1 \omega} \right],$$

where S is the strain rate magnitude and F is the blending function. The coefficient α^* damps the turbulent viscosity causing the low-Reynolds number correction:

$$(2.7) \quad \alpha^* = \alpha_\infty^* \left(\frac{\alpha_0^* + \frac{\text{Re}_t}{6}}{1 + \frac{\text{Re}_t}{6}} \right), \quad \text{Re}_t = \frac{\rho k}{\mu \omega}, \quad \alpha_0^* = \frac{\beta_i}{3}, \quad \alpha_\infty^* = 1, \quad a_1 = 0.31.$$

Since the k - ω model had been modified over the years, the production terms were added to both the k and ω equations, which improved the accuracy of the model for predicting free shear flows. The distribution of turbulent kinetic energy and the specific dissipation rate were described by the equations:

$$(2.8) \quad \rho \frac{\partial k}{\partial t} + \nabla \cdot (\rho k \mathbf{u}) = \nabla \cdot \left(\left(\mu + \frac{\mu_t}{\sigma_k} \right) \nabla k \right) + \tilde{G}_k - \tilde{Y}_k + S_k,$$

$$(2.9) \quad \frac{\partial(\rho\omega)}{\partial t} + \nabla \cdot (\rho\omega \mathbf{u}) = \nabla \cdot \left(\left(\mu + \frac{\mu_t}{\sigma_\omega} \right) \nabla \omega \right) + G_\omega - Y_\omega + D_\omega + S_\omega,$$

where σ_k and σ_ω are the turbulent Prandtl numbers for k and ω , respectively, the production term \tilde{G}_k denotes the generation of turbulence kinetic energy due to the mean velocity gradients, the production term G_ω means the generation of ω , the destruction terms \tilde{Y}_k and Y_ω denote the dissipation of k and ω due to turbulence, respectively, D_ω is the cross-diffusion term, and S_k and S_ω are user-defined source terms. In different regions, β_i from formula (2.7), as well as σ_k and σ_ω , were defined by using the blending function F_1 :

$$(2.10) \quad \beta_i = F_1 \beta_{i,1} + (1 - F_1) \beta_{i,2}, \quad \sigma_k = \frac{1}{\frac{F_1}{\sigma_{k,1}} + \frac{1-F_1}{\sigma_{k,2}}}, \quad \sigma_\omega = \frac{1}{\frac{F_1}{\sigma_{\omega,1}} + \frac{1-F_1}{\sigma_{\omega,2}}}.$$

The constants of the applied turbulence model are as follows: $\beta_{i,1} = 0.075$, $\beta_{i,2} = 0.0828$, $\sigma_{k,1} = 1.176$, $\sigma_{\omega,1} = 2.0$, $\sigma_{k,2} = 1.0$ and $\sigma_{\omega,2} = 1.168$. Other details of the applied turbulence model can be found in [49].

The formulation of the SST k - ω model was enhanced by the intermittency transport equation to evaluate laminar-turbulent transition of the boundary layers of the wall. The intermittency transition model [50] was considered as a further development of the γ - Re_θ transition model [51]. The following transport equation for intermittency γ was used:

$$(2.11) \quad \frac{\partial(\rho\gamma)}{\partial t} + \nabla \cdot (\rho\gamma\mathbf{u}) = \nabla \cdot \left(\left(\mu + \frac{\mu_t}{\sigma_t} \right) \nabla \gamma \right) + P_\gamma - E_\gamma.$$

The boundary condition for γ is zero normal flux on the aortic wall, while the value of γ is equal to 1 on the inlet. The transition and relaminarization source terms were defined as follows:

$$(2.12) \quad P_\gamma = F_{\text{length}}\rho S\gamma(1 - \gamma)F_{\text{onset}},$$

$$(2.13) \quad E_\gamma = c_{a2}\rho\Omega\gamma F_{\text{turb}}(c_{e2}\gamma - 1),$$

where S is the strain rate magnitude and Ω is the magnitude of the absolute vorticity rate. The formulation of the function F_{onset} , which was used to activate the source term (2.12), included the ratio of the local vorticity Reynolds number to the critical Reynolds number. Unlike the γ - Re_θ transition model, the critical Reynolds number was not computed from the transport equation, but was obtained algebraically. The function F_{turb} , the local vorticity Reynolds number Re_ν and the constants of the intermittency model were defined as follows:

$$(2.14) \quad F_{\text{turb}} = e^{-\left(\frac{\text{Re}_t}{2}\right)^4}, \quad \text{Re}_\nu = \frac{\sigma d_w^2 S}{\mu\omega}, \quad F_{\text{length}} = 100,$$

$$c_{e2} = 50, \quad c_{a2} = 0.06, \quad \sigma_\gamma = 1.0,$$

where d_w is the wall distance. The details of the intermittency transition model, including experimental correlations of the critical Reynolds number, can be found in [50].

The coupling of the intermittency transition model (2.11)–(2.14) with the SST k - ω model (2.5)–(2.10) was accomplished by modifying the source terms of equation (2.8). The production term \tilde{G}_k was obtained by multiplying γ and the original term of the turbulent kinetic energy equation G_k , which was computed using the Kato–Launder formulation [52]:

$$(2.15) \quad \tilde{G}_k = \gamma G_k = \gamma\mu_t S\Omega.$$

This formulation helps to avoid the excessive levels of the turbulence intensity in stagnation regions. The destruction term \tilde{Y}_k was obtained from the original term Y_k by using the formula:

$$(2.16) \quad \tilde{Y}_k = Y_k \max(\gamma, 0.1).$$

It is worth noting that the production and destruction terms of the ω -equation (2.9) were not modified.

The structural analysis of the aortic valve is aimed to determine the mechanical response of the aortic tissue throughout a cardiac cycle. The aortic valve contains three leaflets that open when the left ventricle of the heart contracts (systole) to eject blood into the aorta. The aortic valve leaflets are attached inside the aortic root, which balloons out around each of the leaflets' attachments, creating the three aortic sinuses. The structural model of the aorta elaborated in the present research involves aortic valve leaflets, Valsalva sinuses and the aortic walls. In spite of variety of results obtained elsewhere, evaluation of mechanical response of patient-specific aortic tissues comprising evaluation of stresses and identification of the exact shape and location of the leaflet surface during blood flow is still a challenging task. Description of mechanical behaviour of aortic tissue follows conventional large strain approach used in nonlinear continuum mechanics. The configuration of a given domain during deformation is assumed to be time-dependent. The formulation of such problems uses a Lagrangian description. Quantities are originally defined in the reference configuration at time instant $t = 0$, while time variation is referred to current configuration at time t . For the sake of clarity, left superscripts 0 and t will denote reference and current configurations, respectively. Consequently, the position of a material point in the reference configuration is denoted by 0x_i , while current position is tx_i . The solid body motion is characterised by the displacement vector ${}^tu_i = {}^tx_i - {}^0x_i$.

Although detailed studies [18] indicate presence of dynamic and hysteric effects even under moderate loads, the quasi-static formulation of structure model is sufficient in many cases, see [18, 45, 53]. The mathematical model of the quasi-static deformation of the structure domain at time instant t is described by the momentum equation. This equation differs from that of fluid (2.1)–(2.3), and it can be written as follows:

$$(2.17) \quad \nabla \cdot {}^t\boldsymbol{\sigma} = \rho_s \cdot {}^t\mathbf{f}_s,$$

where ${}^t\boldsymbol{\sigma}$ denotes the Cauchy stress tensor, considered in the configuration t , $\nabla \cdot$ is the tensor divergence operator, vector ${}^t\mathbf{f}_s$ presents body force and ρ_s is the constant density.

Commonly used boundary conditions were applied in structural model. Firstly, a relatively conservative choice of kinematic boundary conditions, restricting the normal component of the displacement on the base of the structure

at the basal cut plane, was used. Internal surfaces of the aorta leaflets were loaded by the time-dependent fluid pressure. The quasi-static loading predefined character of constitutive model. By typical thermo-dynamical considerations, the Cauchy stress tensor was then obtained by differentiating a pseudo-strain energy W with respect to strain.

In summary, the soft aortic tissue, including both aortic valve walls and its leaflets, was considered as a transversally isotropic and nearly incompressible solid by applying hyper-elastic Fung-type constitutive model [19]. A strain energy potential function U was defined as a function of suitable components E_{ij} of the Green–Lagrange strain tensor:

$$(2.18) \quad U = \frac{c_h}{2}(e^Q - 1) + \frac{1}{2}K(J - 1)^2,$$

where

$$(2.19) \quad Q = b_1 E_{11}^2 + b_2 (E_{22}^2 + E_{33}^2 + E_{23}^2 + E_{32}^2) + b_3 (E_{12}^2 + E_{21}^2 + E_{13}^2 + E_{31}^2),$$

while C_h , b_1 , b_2 , b_3 are the model parameters, $K = 2/d$ is the bulk modulus, d is material incompressibility parameter, $J = \det(\mathbf{F})$ is the volume change, \mathbf{F} is the deformation gradient, $\bar{\mathbf{F}} = J^{-1/3}\mathbf{F}$ is the deformation gradient with the eliminated volume change, and $\bar{\mathbf{B}} = \bar{\mathbf{F}} \cdot \bar{\mathbf{F}}^T$ is the deviatoric stretch matrix (the left Cauchy–Green strain tensor).

3. A description of the patient-specific problem

The complex geometry of the aortic valve is composed of three leaflets attached to the aortic root. Behind them, three anatomic dilatations make the Valsalva sinuses. The new geometrical model was proposed to simplify a mathematical description of the aortic valve by reducing the number of parametric curves and retaining the required accuracy. A critical prerequisite for the patient-specific analysis of the aortic valve was the integration of the state-of-the-art clinical imaging with biomechanical computations. The altered blood flow dynamics past the aortic valve might be an important factor, causing complications in the ascending aortic root in patients.

The patient-specific geometry of the aortic valve was obtained from electrocardiographically gated 4D images that were acquired from a human subject by using the Philips iE33 ultrasonographic system (Philips Healthcare, Andover, MA, USA). The acquired DICOM images were converted from polar coordinates to Cartesian coordinates by using the plugin of QLAB-v9.0 (Philips Healthcare, Andover, MA, USA) quantification software. The medical imaging interaction toolkit (MITK) [54] was employed to obtain the geometric parameters of the aortic sinuses, valve leaflets and ascending aorta from the medical images (Fig. 1).

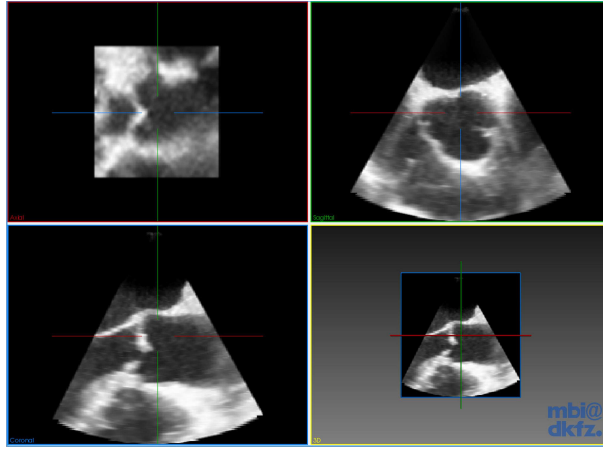


FIG. 1. The image analysis using medical imaging interaction toolkit.

The 3D images of the closed aortic valve were selected from the subject’s data set at the end of the diastole for extracting the main geometric parameters.

A 3D geometric model was constructed from the parametric curves according to the extracted patient-specific geometric parameters. The 3D surface model of sinuses was based on the extrusion of the curtate epicycloid parametric curve [55] as follows:

$$(3.1) \quad x = (a + b) \cos t + \lambda(z)b \cos \frac{(a + b)t}{b}, \quad \frac{a}{b} = 3, \quad 0 < \lambda(z) < 1,$$

$$(3.2) \quad y = (a + b) \sin t + \lambda(z)b \sin \frac{(a + b)t}{b}, \quad \frac{a}{b} = 3, \quad 0 < \lambda(z) < 1,$$

where a is the radius of the aortic root scaled by the parameter $\lambda(z)$, $0 \leq z \leq 1$, which must be fitted to real geometry (Fig. 2a), b is a small radius of the epicycloid forming surface of sinuses and t is the parameter varying from 0 to 2π .

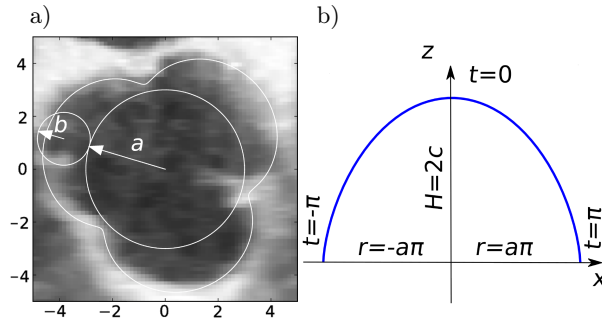


FIG. 2. Parametric curves: a) the epicycloid of sinuses, b) xz projection of the cycloidal type surface of revolution.

The analytical surface model of the valve leaflets is based on the cycloidal-type surfaces of revolution [56] (Fig. 2b), whose mathematical expression is defined as follows:

$$(3.3) \quad x = a'(t + \sin t) \cos \varphi = r(z) \cos \varphi,$$

$$(3.4) \quad y = a'(t + \sin t) \sin \varphi = r(z) \sin \varphi,$$

$$(3.5) \quad z = c(1 + \cos t) = z,$$

$$(3.6) \quad r(z) = a' \left[\frac{\sqrt{z(2c - z)}}{c} + \arccos\left(\frac{z}{c} - 1\right) \right],$$

where a' is the radius of the leaflet surface of the aortic valve, c is the half-height of the sinus root, $r(z)$ is the radius of the revolution surface, t is the parameter varying from $-\pi$ to π , and φ is the angle, which varies from 0 to 2π .

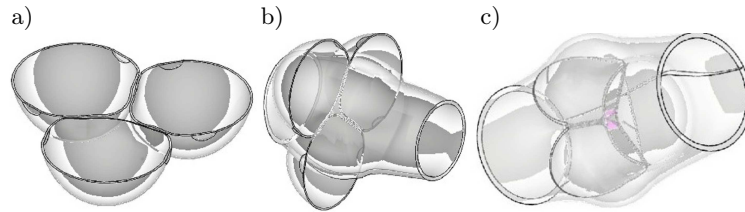


FIG. 3. The geometric model: a) the cycloid revolution surfaces after overlapping, cutting and smoothing, b) the curtate epicycloid extraction and cycloid revolution before cutting, c) the final geometry of the aortic sinuses and the valve.

The patient-specific geometry of the aortic valve was defined by NURBS surfaces generated in Salome 7.6.0 (OPEN CASCADE SAS, Guyancourt, France). Boolean cutting and joining operations were performed to combine the NURBS surfaces into the final geometry. Figure 3 presents the separate parts of the CAD model of the analytically described aortic valve. Figure 3a shows the cycloid revolution surfaces after overlapping, cutting and smoothing. Figure 3b presents the curtate epicycloid extraction and cycloid revolution (before cutting). Figure 3c shows the final geometry of the aortic sinuses and the valve. The patient-specific geometry was imported into the ANSYS DesignModeler [57] to generate the finite element (FE) meshes and finite volume meshes for a solid and a flow, respectively.

The systolic phase of the cardiac cycle was analysed by applying the time-dependent plug flow as the inflow boundary condition. According to the experimental data, the mass flow rate was equal to 0.40 kg/s, which was equivalent to 1.41 m/s velocity at the peak systole. All simulations started from a zero flow initial condition and the prescribed inflow was accelerated according to the measured waveform shown in Fig. 4. The turbulence intensity of 5% and the

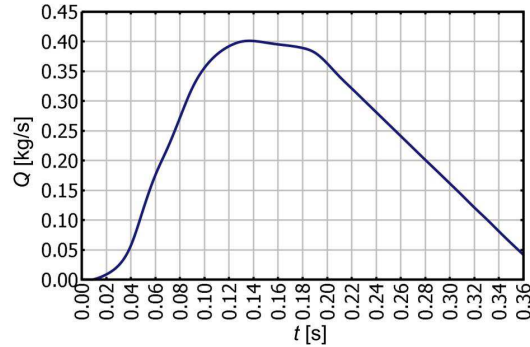


FIG. 4. The mass flow rate specified on the inlet.

hydraulic diameter equal to 0.018 m were specified on the inlet. On the outlet, the prescribed pressure and zero velocity gradient normal to the boundary were applied to allow the vortices shed by the leaflets exit the computational domain with minimal disturbances. The no-slip boundary conditions were prescribed for velocity on the aorta walls and leaflet surfaces.

4. The numerical model

4.1. Discretisation approach and numerical details

The differential flow equations (2.1)–(2.3), (2.8)–(2.11) were solved by the finite volume method on collocated grids [57]. The pressure-based solver with the first-order implicit transient formulation was used for fluid simulations. The under-relaxation of equations, also known as implicit relaxation, is used in the pressure-based solver to stabilise the convergence behaviour of the outer non-linear iterations by introducing selective amounts of variables in the system of discretized equations. The default value of 0.75 of the under-relaxation factor was selected for the pressure and velocity components. The coupled solution of the momentum and continuity equations was considered to accelerate the convergence of the numerical computations. Application of the coupled scheme could be advantageous in the cases of patient-specific aortic valves with complex native geometries, lower mesh quality, and large number of expensive nonlinear iterations and poor convergence of the numerical solution. Gradients were evaluated by using the least squares cell-based scheme to ensure sufficient accuracy on unstructured meshes with skewed and distorted finite volumes. The second-order upwind scheme was applied to discretize the convective terms in momentum equations. The second-order accurate pressure discretization scheme was used to reduce the number of nonlinear iterations. The blood was modelled as an incompressible Newtonian fluid with the density set to $\rho = 1060 \text{ kg/m}^3$.

The dynamic viscosity coefficient was $\mu = 0.004028 \text{ kg}/(\text{m} \cdot \text{s})$. For structural analysis, the material of the solid part with the specific weight of $1000 \text{ kg}/\text{m}^3$ was considered.

A mathematical model (2.17) of the structural part, including Valsalva sinuses and the aortic walls, was solved by using one of the most popular methods, called the finite element method (FEM). Large deformation problem, taking into account material transversally isotropic model (2.18), (2.19), could be expressed for FE e in incremental way:

$$(4.1) \quad [M^e]^e \{^{t+\Delta t} \ddot{u}^e\} + ([^t K_L^e] + [^t K_{NL}^e(\{u^e\})]) \{\Delta u^e\} = \{^t F^e\},$$

where $\{\Delta u^e\}$ means change of displacement in the interval between t and $t + \Delta t$, $[M^e]^e$ is mass matrix, $[^t K_L^e]$ and $[^t K_{NL}^e(\{u^e\})]$ – are linear and nonlinear parts of stiffness matrix, and $\{^t F^e\}$ is loading. The solid second-order tetrahedral elements SOLID187 with 10 nodes, having translations in the nodal x , y and z directions, were used for the FE computations performed by ANSYS [57].

The model (2.18), (2.19), was used to fit the circumferential and radial stress-strain data of the aortic valve leaflet obtained from tensile tests [40]. The parameters of the model (2.18), (2.19), were identified using “curve fitting” with experimental data module available in ANSYS, and a good fit was found with parameters equal to $C_h = 589 \text{ kPa}$, $b_1 = 4.19$, and $b_2 = 0.299$. Since b_3 could not be obtained by the tensile test, it was assumed to be equal to b_2 [58].

4.2. The solution procedure

Initially, the geometry of the aortic valve was reconstructed from parametric curves according to the electrocardiographically gated images that were acquired from a human subject at the end of the diastole. According the patient-specific geometry, the FE meshes and finite volume meshes were generated for a solid and a flow to have the conforming boundary. The structural analysis was performed by using the finite element method to determine the stress-strain state of the aortic valve and to obtain the positions of opened valve leaflets at the peak systole. Several ways to load the aortic valve leaflets were investigated. The results obtained applying the pressure drop, relevant to the peak systole conditions, were compared with those computed by using the pressure and viscous force extracted from the preliminary CFD solution. The pressure and viscous force values were mapped from the fluid mesh cells handled by ANSYS Fluent into the solid mesh nodes handled by ANSYS Mechanical APDL on the leaflet surfaces by using “Surface FSI Mapping” facilities for one-way flow-structure interaction.

The haemodynamic analysis of systolic turbulent flow through aortic valve was performed by using the finite volume method. The research was focused on the flow, close to the peak systole, because of the highest pressure gradients that

are measured during the peak systole in the clinical practice. The geometry of the already opened valve was imported from the structural analysis to weaken coupling of structural and CFD solvers, to reduce the following deformations of fluid mesh and to save computational resources. Thus, the solution domain and the resulting finite volume mesh were allowed to move only in the time interval, enclosing the peak systole, and were fixed in the remaining parts of the time range to avoid expensive remeshing and relevant convergence issues. The moving boundary update was performed transferring the displacements from the structural analysis to the fluid mesh nodes by the smart bucket algorithm [57]. The applied algorithm generated interpolation weights that were ideal for transferring the profiles of non-conserved quantities from a source mesh to a target mesh. In moving boundary zones, enclosing valve leaflets, the diffusion-based smoothing [57] of the finite volume meshes was applied. The mesh motion was governed by the Laplace equation, preserving the number of nodes and the mesh topology. The diffusion coefficient was a function of the cell volume to control how the boundary motion diffuses into the interior of the domain. Larger cells were caused to absorb more of mesh motion, preserving the quality of smaller cells. Two or three iterations of uncoupled solvers with the relevant load and displacement transfer were performed to eliminate large changes in numerical solutions, because the movement of the opened aortic valve leaflets was very small after the peak systole. The main outcome of haemodynamic analysis was a comparative study of various turbulence models for the pulsatile transitional aortic valve flows, including the low-Reynolds number turbulence.

5. The numerical results

A critical prerequisite for patient-specific analysis of the aortic valve was the integration of state-of-the-art clinical imaging with biomechanical computations. Pre-processing, visualization and all computations were performed on the Open-Stack cloud infrastructure hosting software services [59–61] for patient-specific numerical analysis of the aortic valve flows.

5.1. The finite element analysis of the stress-strain state of the aortic valve

The structural model for determining the stress-strain state was constructed. The structural problem was solved according to the principles of the standard FEA, where three FE meshes of various densities were generated. The smallest elements were obtained near the surface of the valve leaflets, called commissures. The models, consisting of the 94 808, 190 805 and 410 502 FEs and having 2, 4 and 5 FEs per leaflet thickness, respectively, were constructed and verified. The aortic valve leaflets were loaded by the pressure drop relevant to the peak systole conditions ($t = 0.140$ s). Two cases of the pressure load were considered:

Case 1: $p(t) = p_1(t) - p_2(t)$ pressure load, varying in time.

Case 2: load, varying in time and space.

The Case 1 pressure load was described by the analytical pressure curves (Fig. 5a) applied on surfaces of the valve leaflets. The curve from inlet side was denoted as p_1 curve, which reached maximum at physiological conditions of healthy patient (120 mmHg). The curve p_2 , applied from the opposite side, caused maximum pressure drop equal to 1500 Pa. The Case 2 load was extracted from the preliminary CFD solution obtained by using the ANSYS Fluent (Figs. 6a and 6b). The pressure and viscous force were mapped from the fluid onto the leaflet surfaces, associated with a FE mesh for structural analysis, by using “Surface FSI Mapping” facilities of ANSYS Fluent. Initially, the values of the variables available on cell centroids were calculated on the nodes of the finite volume mesh. The 0th-order interpolation was applied to provide target node values using the source data. Finally, load files were written for the uncoupled FEM analysis of aortic valve displacements and deformations, performed by using the ANSYS Mechanical APDL. Although haemodynamic stresses were shown to regulate valvular biology, the native wall shear stress experienced by

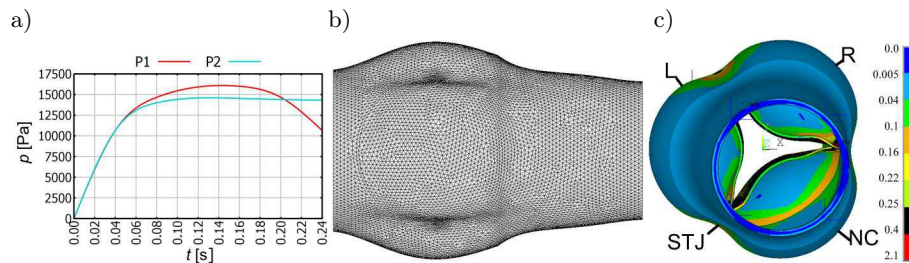


FIG. 5. Description of Case 1: a) analytical pressure curves, b) illustration of the fine FE mesh (410 502 FEs), c) distribution of the equivalent (von Mises) stress (in MPa).

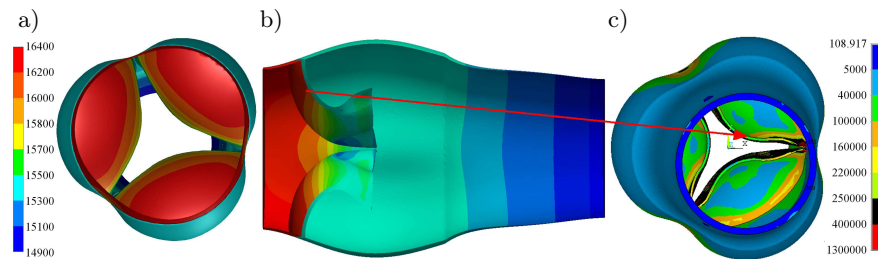


FIG. 6. Description of Case 2: a) transversal view of the pressure distribution (in Pa) computed by using CFD analysis, b) longitudinal view of the pressure distribution on the wall surfaces of the aortic valve, c) distribution of the equivalent (von Mises) stress (in Pa) at the peak systole (red arrow shows position of the leaflet bell).

the aortic valve leaflets remained largely unknown [44]. Accordingly, Case 2 was divided into two subcases:

Case 2-1: only pressure was mapped.

Case 2-2: pressure and viscous force were mapped to take into account the wall shear stress.

The solution of the nonlinear large deformation problem (4.1) was performed in an iterative manner by using the program-controlled time substep size, with the smallest size $\Delta t_{\min} = 1 \cdot 10^{-8}$ s. The preconditioned conjugate gradient iterative solver, using full Newton–Raphson schema, was considered. Some difficulties of convergence were avoided when an automatic asymmetric frictionless contact pair was selected. The augmented Lagrange method with penetration tolerance 0.10 was the most successful.

Table 1. Summary of structural analysis results.

Parameter	Model			
	Case 1		Case 2-1	Case 2-2
	Coarse mesh	Fine mesh		
von Mises stress, MPa maximum	1.42	2.11	1.37	<u>1.39</u>
In leaflet bell	0.39	0.40	0.36	0.37
Displacement, mm maximum	6.04	6.81	6.89	<u>7.33</u>

The results referring to the stress-strain state in the peak systole are presented as the equivalent (von Mises) stress on deformed state in Fig. 5c. The results obtained for different load cases are presented in Table 1. The Case 1 load revealed the results of von Mises stress, which reached the maximum value of 1.42 MPa at the commissures of leaflets for the coarse FE mesh and 2.11 MPa for the fine FE mesh near the stress concentration area (Fig. 5c). In Case 2-1, the stresses only reached 1.37 MPa (Fig. 6c), while the load in Case 2-2 produced stress values of 1.39 MPa. Thus, 3% stress increase could be observed in the leaflet bell zone. It is worth noting that the computed stresses had the values similar to those found in STURLA *et al.* [62], where the reported stresses varied from 0.3 to 0.4 MPa.

In case of the pressure drop at the peak systole conditions, there was a noticeable asymmetry of in-plane distribution of the maximal principal stress among the leaflets and regional variation of the stress on each leaflet. Variation of principal stress vectors (which is not presented) was parallel to radial direction, which mimicked the reorientation of fibre directions. Maximum principal stresses were 0.065, 0.064 and 0.061 MPa on the non-coronary (NC), right (R) and left (L) leaflet, respectively. Differences between stresses, acting on the three sinuses of

the aortic root, were less relevant. Their average values were equal to 0.189, 0.188 and 0.186 MPa on the right, non-coronary and left sinus, respectively. In the region above the left and non-coronary sinus, in the so-called sinotubular junction (STJ), the maximum circumferential and longitudinal stresses of the aortic wall were 0.355 and 0.324 MPa, respectively. Above the right sinus they were equal to 0.340 and 0.300 MPa.

Different load scenarios caused different maximum values of total displacements as well as different distribution of the displacement field. Figures 7a and 7b show the distribution of displacements at the peak systole conditions in case of mild aortic valve stenosis. Displacements are investigated in three selected points of NC leaflet: the first point is placed in the commissure, the second point is located in the bell region, and the third point is considered near the leaflet attachment with aortic root, in the so-called base region. In Fig. 7, arrows visualize the displacement vector of the first point. In Case 1, the displacements of the first point $u_{1, \text{Case 1}} = 0.00491$ m are 30% less than the maximal values

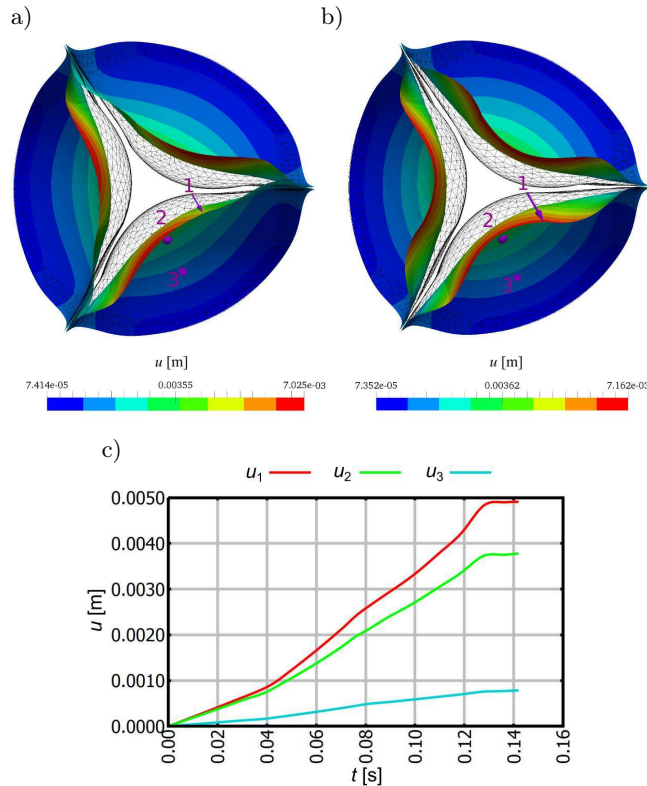


FIG. 7. Total displacements of the outer (ventricular) leaflet surfaces (undeformed surfaces are showed by mesh): a) for Case 1, b) for Case 2, c) temporal variation of the displacements of the selected points for Case 1.

$u_{\max, \text{Case 1}} = 0.00703$ m that are observed in the other location. In Case 2, the maximal values of displacements $u_{1, \text{Case 2}} = u_{\max, \text{Case 2}} = 0.00716$ m are obtained in the first point. In Case 1, displacement values of the second point and third point are equal to $u_{2, \text{Case 1}} = 0.00378$ m and $u_{3, \text{Case 1}} = 0.00078$ m, respectively. These values are 16% and 3% less than the displacements of the second point and third point in Case 2, respectively. Figure 7c shows the temporal variation of displacements of the three considered points. It is obvious that displacements of the third point at the leaflet base are significantly smaller than that of the first point and second point. It was also observed that the increment of displacements of aortic valve leaflets decreased in the short time interval near the peak systole.

In Case 2, a pressure obtained from the patient-specific CFD computations was different on each leaflet, which caused asymmetry in the displacement field. Wall shear stresses increased the displacements by 6% and affected the cross-sectional area of the flow jet at the vena contracta.

5.2. The analysis of the turbulent aortic valve flow

The haemodynamic analysis was performed to assess the turbulent blood flow past the aortic leaflets. The patient-specific geometry obtained from the electrocardiographically gated images was employed for the finite volume analysis of the aortic valve [59]. The solution domain was discretized by meshes, containing from 1.25 to 1.78 million of finite volumes. The resulting distance of the first volume centre from the wall ranged from $1.2 \mu\text{m}$ to $90.1 \mu\text{m}$. Figure 8 shows the complex 3D flow patterns at $t = 0.165$ s in the longitudinal section of aortic sinuses. The velocity field was visualized by using streamlines coloured according to the pressure field. It is worth noting that the velocity field at $t = 0.165$ s acquired the oscillating character because of turbulent effects, following the peak systole ($t = 0.140$ s). Thus, a turbulence model was required to damp oscillations and to avoid the divergence of the solution.

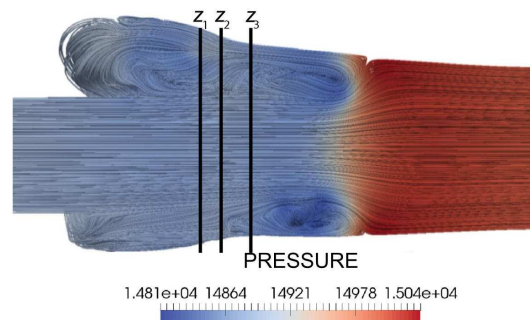


FIG. 8. Pressure field and streamlines of a complex flow pattern at $t = 0.165$ s in the aortic sinuses.

Figure 9 shows the distribution of the gauge pressure at $t = 0.124$ s in vertical cross-sections of the aortic sinuses, when the accelerating flow through the aortic valve approaches the peak systole. The position of three scaled cross-sections at the coordinates $z_1 = 0.021$ m, $z_2 = 0.025$ m and $z_3 = 0.030$ m are marked by lines in Fig. 8. The colour map visualizes the distribution of the pressure field, revealing a complex flow pattern with vortices following the open valve in Fig. 9. Larger vortices are formed in the aortic sinuses, while smaller vortices develop behind the junctions of these sinuses. It is worth noting that the high Reynolds number $k-\varepsilon$ turbulence model significantly smoothes the vortex field (Fig. 9b). The results of the SST $k-\omega$ model (Fig. 9c) are closer to the laminar flow (Fig. 9a). Thus, the detailed investigation and comparison of turbulence models is necessary for the haemodynamic analysis of the aortic valve because the applied model can have a strong influence on the distribution of the pressure field and the resulting flow pattern.

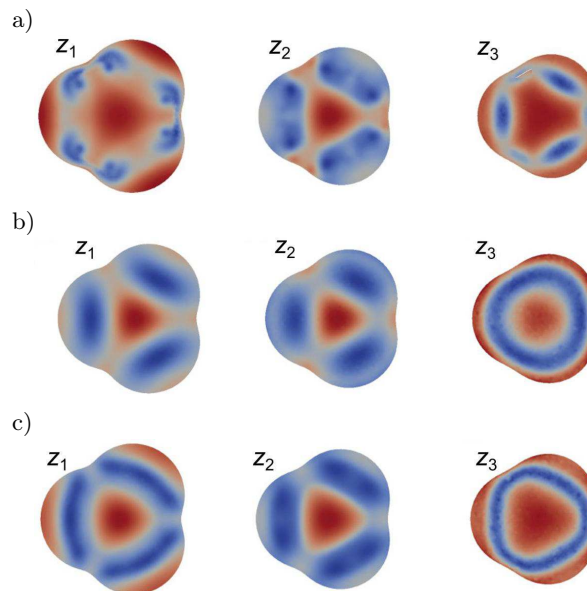


FIG. 9. Distribution of the pressure field in vertical cross-sections ($z_1 = 0.021$ m, $z_2 = 0.025$ m, $z_3 = 0.030$ m) of the aortic sinuses at $t = 0.124$ s: a) a laminar flow, b) the $k-\varepsilon$ turbulence model, c) the SST $k-\omega$ turbulence model.

In the present research, various modifications of the $k-\omega$ model were investigated to evaluate the effects of the low Reynolds number turbulence in the pulsatile aortic valve flow. Figure 10 presents the values of turbulent variables plotted on a line segment ($z = 0.040$ m). The curve “ke” denotes the results yielded by the standard $k-\varepsilon$ turbulence model. The curves “ko”, “ko-sst”, “ko-re”, “ko-cv” and “ko-itr” present the results obtained by using the standard $k-\omega$ model,

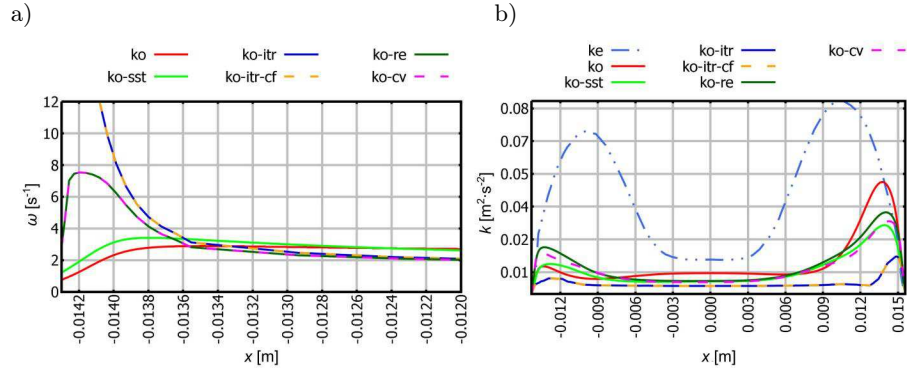


FIG. 10. Distribution of turbulent variables on the line segment placed at $z = 0.040$ m: a) turbulent dissipation rate in the case of the accelerating flow $t = 0.080$ s, b) turbulent kinetic energy at the peak systole, when $t = 0.140$ s.

the SST k - ω model (2.5)–(2.10), the SST k - ω model with the low Reynolds number correction (2.7), the SST k - ω model with the low Reynolds number correction and curvature correction, as well as the SST k - ω model enhanced by the intermittency transition equation (2.11), respectively. The transitional turbulence model based on the intermittency transition equation includes the corrections of the low Reynolds number, the curvature and cross flow transition. The transition model, which does not evaluate the cross-flow transition, was also investigated, but the curves “ko-itr-cf”, representing the results yielded by it, completely overlapped the “ko-itr” curves. Therefore, the results obtained without taking into account the cross-flow transition are not shown in some figures. Figure 10a shows the values of the specific dissipation rate in the case of the accelerating flow, when $t = 0.080$ s. The intermittency transition model (2.11)–(2.14) yields very high values of the specific dissipation rate in the laminar layer near the wall. The standard k - ω model gives the lowest values of the specific dissipation rate in the case of the accelerating flow. Figure 10b presents the distribution of turbulent kinetic energy at the peak systole, when $t = 0.140$ s. All k - ω models generate significantly lower kinetic energy values than the k - ε model. It is worth noting that the values of the SST k - ω model enhanced by intermittency transition equation are the lowest.

Figure 11 shows the distribution of turbulent viscosity in the case of the peak systole, when $t = 0.140$ s. The main flow and two large vortices resulted in three peaks of turbulent viscosity values that can be clearly seen in the curve “ke” of the k - ε model. All k - ω models generated much lower turbulent viscosity, but the turbulent viscosity values of the standard k - ω model most closely matched those of the k - ε model. The lowest turbulent viscosity values of the SST k - ω were obtained using the intermittency transition model, and this resulted in

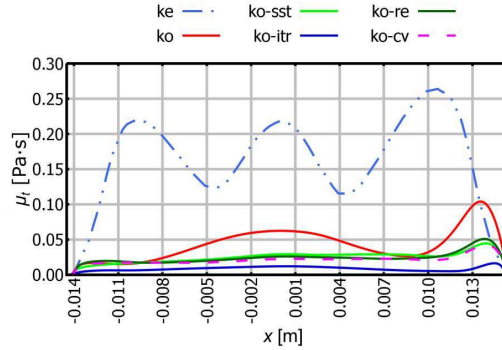


FIG. 11. Turbulent viscosity values on a line segment ($z = 0.040$ m) in the case of the peak systole, when $t = 0.140$ s.

the lowest diffusion of laminar flow vortices. Other variants of $k-\omega$ turbulence models produced slightly different turbulent viscosity values, but the curve “ko-cv”, representing the SST $k-\omega$ model with the low Reynolds number correction and curvature correction, most closely matched the curve “ko-itr”.

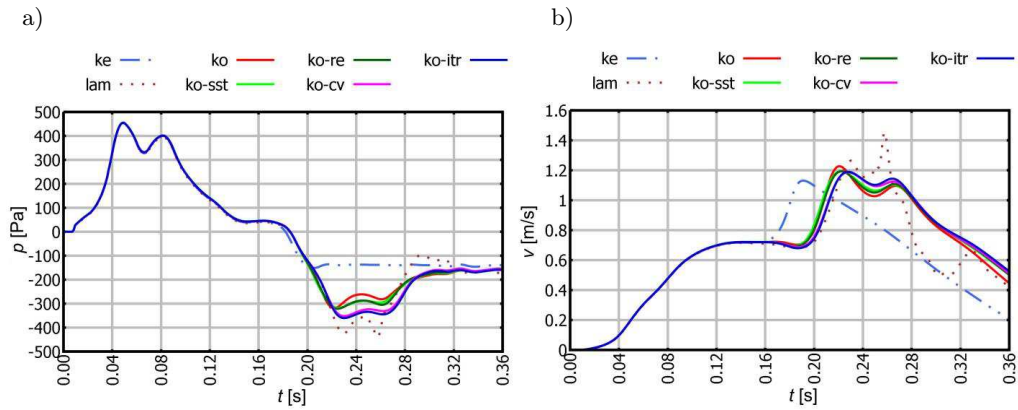


FIG. 12. Time evolution of the variables at the point with the coordinates $x = 0.000$ m, $y = 0.000$ m, $z = 0.070$ m: a) pressure, b) z velocity component.

Figure 12 presents time evolution of the pressure and z velocity component at the centreline point with the coordinates $x = 0.000$ m, $y = 0.000$ m, $z = 0.070$ m. The laminar solution had an oscillating nature in the case of both variables. The application of the $k-\varepsilon$ model resulted in an overdiffusive solution. The results yielded by the $k-\omega$ models were much closer to the laminar solution. In most cases, the SST $k-\omega$ model enhanced by intermittency transition produced the lowest turbulent viscosity values (Fig. 10); therefore, its solution most closely

matched the laminar one. It is worth noting that the curve “ko-cv” was closer to the curve “ko-itr” than the other ones. Therefore, the SST $k-\omega$ model with the low Reynolds number correction and curvature correction can also be useful for predicting the velocity and pressure fields.

Figure 13 presents time evolution of the accumulated iteration number (AIN), which illustrates the convergence rate of the numerical solution. Only a part of the time interval was considered to make the differences between the curves more obvious. The laminar solution revealed the slowest convergence caused by small diffusion terms relevant to higher Reynolds numbers. Moreover, the laminar solution did not converge from the time instance $t = 0.288$ s. Rather unexpectedly, convergence of the $k-\varepsilon$ model was slower than that of the $k-\omega$ models. The simplest $k-\omega$ model (the curve “ko”) allowed for achieving the fastest convergence, while other $k-\omega$ models demonstrated similar convergence rates. At the considered scale, the curves “ko-re”, “ko-itr” and “ko-itr-cf” nearly overlapped, which indicates almost identical convergence rates.

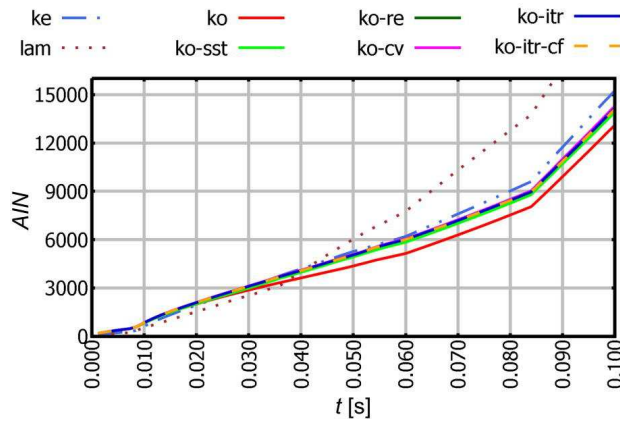


FIG. 13. Solution convergence of different turbulence models.

Figure 14 shows time evolution of pressure differences between the laminar and turbulent solutions. Each curve represents the difference between the laminar flow pressure p_{lam} and the turbulent flow pressure p_{tur} obtained by using the particular turbulence model in L_2 norm $E = \|p_{\text{lam}} - p_{\text{tur}}\|_2$, which shows medium variation of the pressure differences in the solution domain. It is evident that the difference between the results obtained by using the $k-\varepsilon$ model and the laminar flow is the largest. The results yielded by all $k-\omega$ models are closer to the laminar solution, which is natural for low Reynolds number turbulence flows. In most of the time instances, the $k-\omega$ with intermittency transition model revealed the smallest difference. Its curve “ko-itr” was identical to the curve “ko-itr-cf” of the

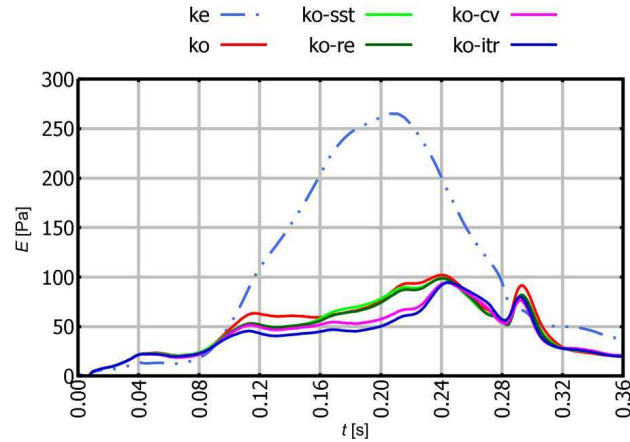


FIG. 14. Time evolution of pressure differences between the laminar and turbulent solutions in L_2 norm.

same model, which did not evaluate the cross-flow transition. Therefore, it can be concluded that the influence of the cross-flow transition is not significant in the investigated aortic valve flows.

6. Conclusions

The computational analysis of the patient-specific aortic valve is presented. The proposed 3D geometric model based on the parametric curves and on the resulting NURBS surfaces is close to the aortic valve anatomy. Therefore, it can be effectively used for quantitative representation of the native valve structures. The computed values of von Mises stress are in agreement with the results reported in the literature. Physiological pulsatile flow conditions and complex 3D blood flow patterns of the aortic valve caused the oscillating laminar solution and convergence difficulties at the end of the flow deceleration phase. The applied turbulence models help to damp oscillations and improve the convergence of the solution. However, the standard k - ε turbulence model significantly smoothes the vortex field. The shear-stress transport k - ω model supplemented with the intermittency transition equation revealed the lowest diffusion of the laminar flow vortices and the smallest differences between the solutions of the laminar and turbulent flows. This model seems to be best suited for adequate modelling of the turbulent and transitional flows through the aortic valve. The performed quantitative comparison of the numerical solutions has shown that the influence of the cross-flow transition can be neglected in the case of the investigated flow conditions. However, using the low Reynolds number correction and curvature correction of the k - ω turbulence models can be rather important.

Acknowledgements

This research was supported by the Research Council of Lithuania within the framework of the project “Patient-specific simulation of the flow through the aortic valve” (MIP-052/2014).

References

1. EUROSTAT, *Eurostat regional yearbook 2014*, Publications Office of the European Union, 2014; doi: 10.2785/54486.
2. A. TANDON, P.A. GRAYBURN, *Imaging of low-gradient severe aortic stenosis*, *JACC: Cardiovascular Imaging*, **6**, 184–195, 2013; doi: 10.1016/j.jcmg.2012.11.005.
3. S. ORWAT, G. KALESCHKE, G. KERCKHOFF, R. RADKE, H. BAUMGARTNER, *Low flow, low gradient severe aortic stenosis: diagnosis, treatment and prognosis*, *EuroIntervention*, **9**, Suppl: S38–42, 2013; doi: 10.4244/EIJV9SSA8.
4. J.G. DUMESNIL, P. PIBAROT, B. CARABELLO, *Paradoxical low flow and/or low gradient severe aortic stenosis despite preserved left ventricular ejection fraction: implications for diagnosis and treatment*, *European Heart Journal*, **31**, 281–289, 2010; doi: 10.1093/eurheartj/ehp361.
5. S. HERRMANN, S. STÖRK, M. NIEMANN, V. LANGE, J.M. STROTMANN, S. FRANTZ, M. BEER, S. GATTENLÖHNER, W. VOELKER, G. ERTL, F. WEIDEMANN, *Low-gradient aortic valve stenosis: myocardial fibrosis and its influence on function and outcome*, *Journal of the American College of Cardiology*, **58**, 402–412, 2011; doi: 10.1016/j.jacc.2011.02.059.
6. E. SIROIS, Q. WANG, W. SUN, *Fluid simulation of a transcatheter aortic valve deployment into a patient-specific aortic root*, *Cardiovascular Engineering and Technology*, **2**, 186–195, 2011; doi:10.1007/s13239-011-0037-7.
7. M. NOBILI, U. MORBIDUCCI, R. PONZINI, C. DEL GAUDIO, A. BALDUCCI, M. GRIGIONI, F. MARIA MONTEVECCHI, A. REDAELLI, *Numerical simulation of the dynamics of a bileaflet prosthetic heart valve using a fluid-structure interaction approach*, *Journal of Biomechanics*, **41**, 2539–2550, 2008; doi: 10.1016/j.jbiomech.2008.05.004.
8. Z. MALECHA, Ł. MIROSLAW, T. TOMCZAK, Z. KOZA, M. MATYKA, W. TARNAWSKI, D. SZCZERBA, *GPU-based simulation of 3D blood flow in abdominal aorta using OpenFOAM*, *Archives of Mechanics*, **63**, 137–161, 2011.
9. C. CHNAFA, S. MENDEZ, F. NICOUD, R. MORENO, S. NOTTIN, I. SCHUSTER, *Image-based patient-specific simulation: a computational modelling of the human left heart haemodynamics*, *Computer Methods in Biomechanics and Biomedical Engineering*, **15**, 74–75, 2012; doi: 10.1080/10255842.2012.713673.
10. C.S. PESKIN, *Flow patterns around heart valves: A numerical method*, *Journal of Computational Physics*, **10**, 252–271, 1972; doi: 10.1016/0021-9991(72)90065-4.
11. S.C. SHADDEN, M. ASTORINO, J.-F. GERBEAU, *Computational analysis of an aortic valve jet with Lagrangian coherent structures*, *Chaos: An Interdisciplinary Journal of Non-linear Science*, **20**, 17512-1-17512–10, 2010; doi: 10.1063/1.3272780.

12. J. DE HART, G.W.M. PETERS, P.J.G. SCHREURS, F.P.T. BAAIJENS, *A two-dimensional fluid-structure interaction model of the aortic valve*, *Journal of Biomechanics*, **33**, 1079–1088, 2000.
13. M.A. NICOSIA, R. P. COCHRAN, D.R. EINSTEIN, C. J. RUTLAND, K.S. KUNZELMAN, *A coupled fluid-structure finite element model of the aortic valve and root*, *The Journal of Heart Valve Disease*, **12**, 781–789, 2003.
14. B. SU, L. ZHONG, X.-K. WANG, J.-M. ZHANG, R.S. TAN, J.C. ALLEN, S.K. TAN, S. KIM, H.L. LEO, *Numerical simulation of patient-specific left ventricular model with both mitral and aortic valves by FSI approach*, *Computer Methods and Programs in Biomedicine*, **113**, 474–482, 2014; doi: 10.1016/j.cmpb.2013.11.009.
15. G.P. GURUSWAMY, C. BYUN, *Fluid-structural interactions using Navier-Stokes flow equations coupled with shell finite element structures*, *AIAA Paper*, **93**, 3087, 1993; doi: 10.2514/6.1993-3087.
16. R. ROSZAK, P. POSADZY, W. STANKIEWICZ, M. MORZYŃSKI, *Fluid-structure interaction for large scale complex geometry and non-linear properties of structure*, *Archives of Mechanics*, **61**, 3–27, 2009.
17. Y. BAZILEVS, J.R. GOHEAN, T.J.R. HUGHES, R.D. MOSER, Y. ZHANG, *Patient-specific isogeometric fluid-structure interaction analysis of thoracic aortic blood flow due to implantation of the Jarvik 2000 left ventricular assist device*, *Computer Methods in Applied Mechanics and Engineering*, **198**, 3534–3550, 2009; doi: 10.1016/j.cma.2009.04.015.
18. A. QUARTERONI, T. LASSILA, S. ROSSI, R. RUIZ-BAIER, *Integrated heart – Coupling multiscale and multiphysics models for the simulation of the cardiac function*, *Computer Methods in Applied Mechanics and Engineering*, **314**, 345–407, 2017; doi: 10.1016/j.cma.2016.05.031.
19. Y.C. FUNG, *Biomechanics: Mechanical Properties of Living Tissues*, Springer, New York, 1993.
20. L. TUMONIS, R. KAČIANAUSKAS, A. KAČENIAUSKAS, M. SCHNEIDER, *The transient behavior of rails used in electromagnetic railguns: numerical investigations at constant loading velocities*, *Journal of Vibroengineering*, **9**, 15–20, 2007.
21. B.E. GRIFFITH, *Immersed boundary model of aortic heart valve dynamics with physiological driving and loading conditions*, *International Journal for Numerical Methods in Biomedical Engineering*, **28**, 317–345, 2012; doi: 10.1002/cnm.2543.
22. D. BLUESTEIN, Y.M. LI, I.B. KRUKENKAMP, *Free emboli formation in the wake of bi-leaflet mechanical heart valves and the effects of implantation techniques*, *Journal of Biomechanics*, **35**, 1533–1540, 2002; doi: 10.1016/S0021-9290(02)00093-3.
23. S. MARQUEZ, R.T. HON, A.P. YOGANATHAN, *Comparative hydrodynamic evaluation of bioprosthetic heart valves*, *The Journal of Heart Valve Disease*, **10**, 802–811, 2001.
24. I.R. IONASEC, *Patient-specific modeling and quantification of the heart valves from multi-modal cardiac images*, PhD thesis, Technische Universität München, Lehrstuhl für Informatikanwendungen in der Medizin, 2010.
25. E. VOTTA, T.B. LE, M. STEVANELLA, L. FUSINI, E.G. CAIANI, A. REDAELLI, F. SOTIROPOULOS, *Toward patient-specific simulations of cardiac valves: State-of-the-art and future directions*, *Journal of Biomechanics*, **46**, 217–228, 2013; doi: 10.1016/j.jbiomech.2012.10.026.

26. H. REUL, A. VAHLBRUCH, M. GIERSIEPEN, TH. SCHMITZ-RODE, V. HIRTZ, S. EFFERT, *The geometry of the aortic root in health, at valve disease and after valve replacement*, Journal of Biomechanics, **23**, 181–183, 1990; doi: 10.1016/0021-9290(90)90351-3.
27. M. THUBRIKAR, *The Aortic Valve*, CRC Press, Inc. Boca Raton, 1990.
28. M.R. LABROSSE, C.J. BELLER, F. ROBICSEK, M.J. THUBRIKAR, *Geometric modeling of functional trileaflet aortic valves: Development and clinical applications*, Journal of Biomechanics, **39**, 2665–2672, 2006; doi: 10.1016/j.jbiomech.2005.08.012.
29. T.E. CLAIBORNE, J. SHERIFF, M. KUETTING, U. STEINSEIFER, M.J. SLEPIAN, D. BLUESTEIN, *In vitro evaluation of a novel hemodynamically optimized trileaflet polymeric prosthetic heart valve*, Journal of Biomechanical Engineering, **135**, 2013; doi: 10.1115/1.4023235.
30. J.S. RANKIN, A.F. DALLEY, P.S. CROOKE, R.H. ANDERSON, *A “hemispherical” model of aortic valvar geometry*, Journal of Heart Valve Disease, **17**, 179–186, 2008.
31. R. HAJ-ALI, G. MAROM, S. BEN ZEKRY, M. ROSENFELD, E. RAANANI, *A general three-dimensional parametric geometry of the native aortic valve and root for biomechanical modeling*, Journal of Biomechanics, **45**, 2392–2397, 2012; doi: 10.1016/j.jbiomech.2012.07.017.
32. G. MAROM, H.-S. KIM, M. ROSENFELD, E. RAANANI, R. HAJ-ALI, *Fully coupled fluid-structure interaction model of congenital bicuspid aortic valves: effect of asymmetry on hemodynamics*, Medical and Biological Engineering and Computing, **51**, 839–848, 2013; doi: 10.1007/s11517-013-1055-4.
33. D. BLUESTEIN, S. EINAV, *Techniques in the stability analysis of pulsatile flow through heart valves*, [in:] Biomechanical Systems Techniques and Applications, Vol. II: Cardiovascular Techniques, C. Leondes [Ed.], CRC Press, 2000; doi: 10.1201/9781420049534.CH-04.
34. C. KIRIS, D. KWAK, S. ROGERS, I.-D. CHANG, *Computational approach for probing the flow through artificial heart devices*, Journal of Biomechanical Engineering, **119**, 452–460, 1997; doi: 10.1115/1.2798293.
35. D. BLUESTEIN, E. RAMBOD, M. GHARIB, *Vortex shedding as a mechanism for free emboli formation in mechanical heart valves*, Journal of Biomechanical Engineering, **122**, 125–134, 2000; doi: 10.1115/1.429634.
36. E. TULISZKA-SZNITKO, K. KIELCZEWSKI, *Direct numerical simulation of the Taylor–Couette flow with the asymmetric end-wall boundary conditions*, Archives of Mechanics, **68**, 395–418, 2016.
37. L. GE, S.C. JONES, F. SOTIROPOULOS, T.M. HEALY, A.P. YOGANATHAN, *Numerical simulation of flow in mechanical heart valves: grid resolution and the assumption of flow symmetry*, Journal of Biomechanical Engineering, **125**, 709–718, 2003; doi: 10.1115/1.1614817.
38. M.D. DE TULLIO, L. AFFERRANTE, G. DEMELIO, G. PASCAZIO, R. VERZICCO, *Fluid-structure interaction of deformable aortic prostheses with a bileaflet mechanical valve*, Journal of Biomechanics, **44**, 1684–1690, 2011; doi: 10.1016/j.jbiomech.2011.03.036.
39. L.P. DASI, L. GE, H.A. SIMON, F. SOTIROPOULOS, A.P. YOGANATHAN, *Vorticity dynamics of a bileaflet mechanical heart valve in an axisymmetric aorta*, Physics of Fluids, **19**, 2007; doi: 10.1063/1.2743261.

40. F. AURICCHIO, A. FERRARA, S. MORGANTI, *Comparison and critical analysis of invariant-based models with respect to their ability in fitting human aortic valve data*, *Annals of Solid and Structural Mechanics*, **4**, 1–14, 2012; doi: 10.1007/s12356-012-0028-x.
41. G.A. HOLZAPFEL, R.W. OGDEN, *Constitutive modelling of arteries*, *Proceedings of the Royal Society A: Mathematical, Physical and Engineering Sciences*, **466**, 1551–1597, 2010; doi: 10.1098/rspa.2010.0058.
42. A. GILMANOV, H. STOLARSKI, F. SOTIROPOULOS, *Non-linear rotation-free shell finite-element models for aortic heart valves*, *Journal of Biomechanics*, **50**, 56–62, 2017; doi: 10.1016/j.jbiomech.2016.11.031.
43. G. MAROM, M. PELEG, R. HALEVI, M. ROSENFELD, E. RAANANI, A. HAMDAN, R. HAJ-ALI, *Fluid-structure interaction model of aortic valve with porcine-specific collagen fiber alignment in the cusps*, *Journal of Biomechanical Engineering*, **135**, 2013.
44. K. CAO, M. BUKAČ, P. SUCOSKY, *Three-dimensional macro-scale assessment of regional and temporal wall shear stress characteristics on aortic valve leaflets*, *Computer Methods in Biomechanics and Biomedical Engineering*, **19**, 603–613, 2016; doi: <http://dx.doi.org/10.1080/10255842.2015.1052419>.
45. A. JODA, Z. JIN, A. HAVERICH, J. SUMMERS, S. KOROSSIS, *Multiphysics simulation of the effect of leaflet thickness inhomogeneity and material anisotropy on the stress-strain distribution on the aortic valve*, *Journal of Biomechanics*, **49**, 2502–2512, 2016; doi: 10.1016/j.jbiomech.2016.02.041.
46. D.J. ACHESON, *Elementary Fluid Dynamics*, Oxford University Press, 1990.
47. A. KAČENIAUSKAS, *Development of efficient interface sharpening procedure for viscous incompressible flows*, *Informatica*, **19**, 487–504, 2008.
48. W. NICHOLS, M. O’ROURKE, C. VLACHOPOULOS [Eds.], [with a contribution from] A. HOEKS, R. RENEMAN, *McDonald’s Blood Flow in Arteries: Theoretical, Experimental and Clinical Principles*, 6th Edition, CRC Press, Taylor & Francis Group, 2011.
49. F.R. MENTER, *Two-equation eddy-viscosity turbulence models for engineering applications*, *AIAA Journal*, **32**, 1598–1605, 1994; doi: 10.2514/3.12149.
50. F.R. MENTER, P.E. SMIRNOV, T. LIU, R. AVANCHA, *A one-equation local correlation-based transition model*, *Flow, Turbulence and Combustion*, **95**, 583–619, 2015; doi: 10.1007/s10494-015-9622-4.
51. R.B. LANGTRY, F.R. MENTER, *Correlation-based transition modeling for unstructured parallelized computational fluid dynamics codes*, *AIAA Journal*, **47**, 2894–2906, 2009; doi: 10.2514/1.42362.
52. M. KATO, B.E. LAUNDER, *The modeling of turbulent flow around stationary and vibrating square cylinders*, *Ninth Symposium on Turbulent Shear Flows*, August 16–18, pp. 10.4.1–10.4.6, 1993; doi: 10.1007/s13398-014-0173-7.2.
53. S. SKATULLA, C. SANSOUR, *On a path-following method for non-linear solid mechanics with applications to structural and cardiac mechanics subject to arbitrary loading scenarios*, *International Journal of Solids and Structures*, **96**, 181–191, 2016; doi: 10.1016/j.ijsolstr.2016.06.009.
54. D. MALEIKE, M. NOLDEN, H.-P. MEINZER, I. WOLF, *Interactive segmentation framework of the Medical Imaging Interaction Toolkit*, *Computer Methods and Programs in Biomedicine*, **96**, 72–83, 2009; doi: 10.1016/j.cmpb.2009.04.004.

55. Z. ŠÍR, B. BASTL, M. LÁVIČKA, *Hermite interpolation by hypocycloids and epicycloids with rational offsets*, *Computer Aided Geometric Design*, **27**, 405–417, 2010; doi: 10.1016/j.cagd.2010.02.001.
56. S.N. KRIVOSHAPKO, V.N. IVANOV, *Encyclopedia of Analytical Surfaces*, Springer International Publishing, 2015; doi: 10.1007/978-3-319-11773-7.
57. T. STOLARSKI, Y. NAKASONE, S. YOSHIMOTO, *Engineering Analysis with ANSYS Software*, Elsevier Butterworth-Heinemann, 2007.
58. M.R. LABROSSE, K. LOBO, C.J. BELLER, *Structural analysis of the natural aortic valve in dynamics: from unpressurized to physiologically loaded*, *Journal of Biomechanics*, **43**, 1916–1922, 2010; doi: 10.1016/j.jbiomech.2010.03.020.
59. A. KAČENIAUSKAS, R. PACEVIČ, V. STARIKOVIČIUS, A. MAKNICKAS, M. STAŠKŪNIENĖ, G. DAVIDAVIČIUS, *Development of cloud services for patient-specific simulations of blood flows through aortic valves*, *Advances in Engineering Software*, **103**, 57–64, 2017; doi: 10.1016/j.advengsoft.2016.01.013.
60. A. KAČENIAUSKAS, R. PACEVIČ, M. STAŠKŪNIENĖ, D. ŠEŠOK, D. RUSAKEVIČIUS, A. AIDIETIS, G. DAVIDAVIČIUS, *Private cloud infrastructure for applications of mechanical and dedical engineering*, *Information Technology and Control*, **44**, 254–261, 2015; doi: <http://www.itc.ktu.lt/index.php/ITC/article/view/7379>.
61. R. PACEVIČ, A. KAČENIAUSKAS, *The development of VisLT visualization service in Openstack cloud infrastructure*, *Advances in Engineering Software*, **103**, 46–56, 2017; doi: 10.1016/j.advengsoft.2016.06.012.
62. F. STURLA, E. VOTTA, M. STEVANELLA, C.A. CONTI, A. REDAELLI, *Impact of modeling fluid-structure interaction in the computational analysis of aortic root biomechanics*, *Medical Engineering and Physics*, **35**, 1721–1730, 2013; doi: 10.1016/j.medengphy.2013.07.015.

Received November 25, 2016; revised version April 20, 2017.
